Analysis of Multilayer Infinite Periodic Array Structures with Different Periodicities and Axes Orientations

Arun K. Bhattacharyya, *Senior Member, IEEE*

Abstract—This paper presents a general procedure to analyze a multilayer array structure, where each layer may have different periodicities, different lattice structures, and/or the array axes between the layers may be nonparallel. The procedure involves determination of global cell with a global coordinate system, then computations of local generalized scattering matrices (GSM's) of individual layers followed by modal mapping from local to global GSM's. The global GSM's for individual layers are then combined to characterize the entire structure. The mapping relations are derived for two layers with different lattice structures, different periodicities, and array-axes orientations. Three examples of practical importance are considered to demonstrate the methodology. The first example is a two-layered patch array with different periodicities. The second example is an array of subarrays with several patch elements within a subarray. It is shown that a subarray can be characterized rigorously by characterizing only one element of a subarray instead of analyzing all the elements of the subarray simultaneously. Consequently, analytical and computational complexities reduce considerably. The last example is a patch array loaded with multilayer meander-line polarizer. The patch array and the meander-line array have two different periodicities and the axes are nonparallel. Detailed radiation characteristics of the structure are presented and compared with that of a strip-grid polarizer. Computational advantages of this method are discussed.

Index Terms—Arbitrary lattice, different axes orientation, different periodicity, infinite array, meander-line polarizer, multilayer structures, patch-fed-patch array, scan blindness, strip-grid polarizer, subarrays.

I. INTRODUCTION

MICROSTRIP array antennas are popular for their low fabrication cost, low profile, and lightweight [1]–[3]. For bandwidth enhancement or for dual-band applications, multilayer patch structures have been proposed [4]–[7]. Analyses of multilayer array structures have been reported in the literature using Floquet modal analysis and generalized scattering matrix (GSM) approach [8]. These analyses assume equal cell size (periodicities) for the layers, therefore, the layers have identical Floquet modal functions and, hence, the GSM cascading is straightforward. For many applications, the layers may have different cell sizes. A typical example of this kind is a patch array antenna loaded with a frequency selective surface (FSS). The cell size of the radiating patch layer is generally determined by the maximum scan requirement. On the other hand, cell size of the FSS layer is determined independently by the pass band

and stop-band specifications. This may result in two different cell sizes for the two layers. A more complex multilayer array structure is a patch array loaded with a polarizing screen [9] (this particular example is considered in Section III-C for a detailed analysis). For this structure, the patch layer and the polarizer layer have different cell sizes and the cell orientations are nonparallel between the layers (patch rows and the polarizer grids are not parallel). Analyses of multilayer array structures having different periodicities between the layers have been reported in [10] and [11]. The structure in [11] consists of a dipole array loaded with one layer of strip grids. The formulation assumes that the cell size of the dipole layer is an "integral multiple" of that of the strip-grid layer. No such assumption is made in [10]. However, in both cases the theory is limited to parallel array-axes orientations between the layers.

In this paper, we present a general analysis of multilayer structures. The layers may have different lattice structures (unit cells) with different periodicities and axes orientations. In our analysis, we first obtain the global unit cell. The global unit cell structure is dependent upon the cell structures and the relative array-axes orientations of the individual layers. We then find the GSM's of the individual layers with respect to the global unit cell. Construction of the global GSM for each layer is necessary in order to apply the GSM cascading rule [8] for analyzing a multilayer structure. It is found that a set of local GSM's (GSM's with local unit cell and local coordinate system of an individual layer) can be used to construct the global GSM for that layer. This is possible because a Floquet mode associated with a given lattice structure can represent a Floquet mode associated with a different lattice structure. The mode numbers (modal indexes for two-dimensional periodic structures), however, will be different for the two different lattices. A mapping relation between the modes associated with a local lattice and the global lattice would allow constructing the global GSM for the layer using the elements of local GSM's. We have established such mapping relations for different cases. To find a local GSM of an individual layer, we use Floquet modal analysis and Galerkin's method of moment [12]. Once we find the global GSM's for all the individual layers, we can find the overall GSM of the structure.

To illustrate the methodology, we consider three different examples for analysis. The first example is a two-layer patch array with different periodicities of the layers. The lower layer patches are excited by probe feeds. The input impedances seen by the driven patch elements are determined. The second example is an infinite array of patch subarrays. The impedance matrix of

the subarray elements is formulated, which is essential for designing the feed network. Computed results for three different subarrays are compared with the available results. The third example is a patch array loaded with a two-layer polarizing screen. We present a detailed electrical characteristics including input match, axial ratio bandwidth, and scan performance. Scan blindness phenomena caused by various guided-mode-resonances are explained through Floquet-mode circle diagram. Relative performances of a meander-line polarizer and a strip-grid polarizer are discussed and the important conclusions are outlined at the end.

II. THEORY

We present the analysis of three structures with increasing order of complexity. We first establish the mapping relations between the Floquet modes of a local cell and the global cell and then outline the steps to be followed towards the analysis of the entire structure.

A. Layers with Different Periodicities: Rectangular Lattices

Consider a multilayer array of printed elements as shown in Fig. 1 where the layers have different periodicities. The elements of each layer are aligned row wise along x and column wise along y, forming a rectangular lattice structure. Suppose $[a, b]$ represents the overall periodicity (we will refer to as global periodicity or global cell) of the structure, where a and b are the lowest common multiple (l.c.m.) of the different periods along x and y directions, respectively. In other words, a unit cell of dimensions $a \times b$ will accommodate a finite number of cells of any layer of the multilayer structure. The number of cells will differ, in general, from layer to layer. The Floquet modes supported by the global cell is given by the following vector modal function [12]:

$$\vec{\psi}_{pq}(x, y, z) = \vec{A}_{pq} \exp(-jk_{xp}x - jk_{yq}y) \\ \times \{\exp(-jk_{zpq}z) + \Gamma \exp(jk_{zpq}z)\} \quad (1)$$

where $\vec{A}_{pq}$ is a constant vector. Expressions for $\vec{A}_{pq}$ with respect to the TE_z and TM_z fields are given in [13]. The wave numbers, for rectangular lattice, are given by

$$k_{xp} = (2p\pi + \phi_x)/a \\ k_{yq} = (2q\pi + \phi_y)/b \\ k_{zpq} = \sqrt{k_1^2 - k_{xp}^2 - k_{yq}^2} \quad (2)$$

k_1 is the propagation constant in a given medium. ϕ_x and ϕ_y are the phase increments per unit cell dimension along x and y-directions, respectively. We will use the symbol $\{\phi_x, \phi_y\}$ to represent the above *differential-phase-pair*.

Suppose the above mode in (1) is incident upon the ith patch layer having the local cell size represented by $[a_i, b_i]$. The incident phase differences between two adjacent local elements of the ith layer along x and y directions would be, respectively,

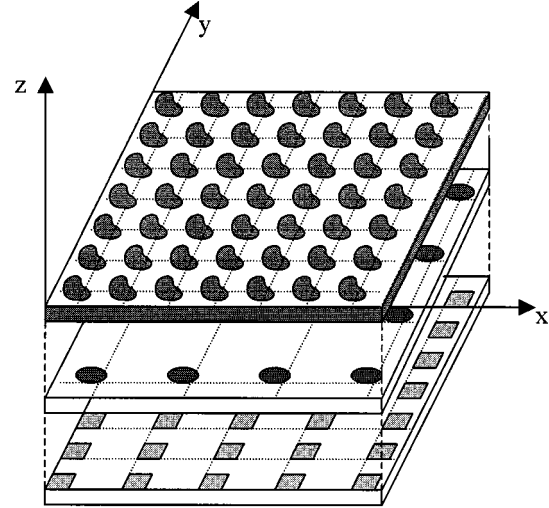$$\phi_{xi} = (2p\pi + \phi_x)a_i/a \\ \phi_{yi} = (2q\pi + \phi_y)b_i/b. \quad (3)$$

Fig. 1.   A three-layered printed array structure with different periodicities and parallel array axes orientations.

The reflected and transmitted modes supported by the ith layer due to the incident field given in (1) can be represented by the following local modal function:

$$\vec{\psi}_{mn}^{(i)}(x, y) = \vec{A}_{mn}^{(i)} \exp\left(-jk_{xm}^{(i)}x - jk_{yn}^{(i)}y\right). \quad (4)$$

The z-dependent factor is suppressed which is unimportant with respect to the present context. The wave numbers in (4) are given by

$$k_{xm}^{(i)} = (2m\pi + \phi_{xi})/a_i \\ k_{yn}^{(i)} = (2n\pi + \phi_{yi})/b_i \quad (5)$$

where m and n are the local mode-index-pair. Henceforth, a Floquet mode with m and n as mode-index pair will be denoted as the (m, n) mode. Substituting ϕ_{xi} and ϕ_{yi} from (3) to (5) we have the following expressions for the wave numbers associated with the reflected and transmitted fields from the ith layer:

$$k_{xm}^{(i)} = \{2\pi(m\alpha + p) + \phi_x\}/a \\ k_{yn}^{(i)} = \{2\pi(n\beta + q) + \phi_y\}/b \quad (6)$$

where

$$a = \alpha a_i \\ b = \beta b_i \quad (7)$$

α and β are integers.

From (6) we notice that when the global (p, q) mode is incident upon the ith layer, the elements of the ith layer will produce the global $(p + m\alpha, q + n\beta)$ modes, where m and n both run from $-\infty$ to ∞. Interestingly, for a single global-mode incidence, the reflected and transmitted global-mode indexes appear only at discrete intervals. These intervals are α and β for x and y indexes, respectively. Furthermore, the global $(p + i\alpha, q + j\beta)$ incident mode (i, j integers) will create the same set of reflected and transmitted modes with different amplitudes. However, the intermediate reflected and transmitted modes will be created if the global incident modes have modal indexes like $(p + i, q + j)$, where $i < \alpha, j < \beta$. The next step is to establish a one-to-one

mapping between the global modal indexes and the local modal indexes of the i-th layer. This mapping relation allows representing the local GSM of the ith layer with respect to the global modal index system. When the individual layer GSM's are represented in terms of a global modal index system, we can directly use the multimode cascading rules [8], [12] to analyze a multilayer structure. The advantages of this procedure will be discussed later.

From (5) and (6) we notice that the $(p + m\alpha, q + n\beta)$ mode in the $[a, b]$ cell is equivalent to the (m, n) mode in $[a_i, b_i]$ cell. The differential-phase pair for the above cells are $\{\phi_x, \phi_y\}$ and $\{(2p\pi + \phi_x)/\alpha, (2q\pi + \phi_y)/\beta\}$, respectively. Therefore, by setting different values of p from zero to $\alpha - 1$ and q from zero to $\beta - 1$, we can cover the entire global modal space using local modes.

From the previous discussion, we can conclude that the local (m, n) mode in the ith layer with a differential-phase pair $\{(2p\pi + \phi_x)/\alpha, (2q\pi + \phi_y)/\beta\}$ is equivalent to the $(p + m\alpha, q + n\beta)$ mode in the $[a, b]$ cell with the differential-phase pair $\{\phi_x, \phi_y\}$. Therefore, to fill in the entire global modal space we have to compute the local GSM's of the ith layer with the following set of differential-phase pairs:

$$\{\phi_{xi}, \phi_{yi}\} = \{\phi_x/\alpha, \phi_y/\beta\}, \{(2\pi + \phi_x)/\alpha, \phi_y/\beta\}$$
$$\{\phi_x/\alpha, (2\pi + \phi_y)/\beta\}, \cdots, \{(2(\alpha - 1)\pi + \phi_x)/\alpha$$
$$(2(\beta - 1)\pi + \phi_y)/\beta\}.$$

The corresponding global mode-index pairs would be

$$(j, k) = (m\alpha, n\beta), (m\alpha + 1, n\beta), (m\alpha, n\beta + 1), \cdots$$
$$((m + 1)\alpha - 1, (n + 1)\beta - 1)$$

where m and n both run from $-\infty$ to ∞. Note that to construct the global GSM for the ith layer, the local GSM's should be computed $\alpha\beta$ number of times. The following simple steps should be followed in order to analyze a multilayered structure with different periodicities.

Step 1) Find $[a, b]$, the global cell size of the structure. $[a, b]$ basically is equal to the l.c.m. of the local cell dimensions of the layers in the structure.

Step 2) Find the global differential-phase-pair $\{\phi_x, \phi_y\}$ from the input excitations or scan direction, etc.

Step 3) Consider a given layer and find the local cell size $[a_i, b_i]$. Find $\alpha = a/a_i$ and $\beta = b/b_i$. Select a differential-phase pair $\{(2p\pi + \phi_x)/\alpha, (2q\pi + \phi_y)/\beta\}$ by selecting a set of p and q, where p should be an integer between zero and $\alpha - 1$ and q should be an integer between zero and $\beta - 1$. Compute the corresponding local GSM. Rename the local GSM element indexes (m, n) globally as $(p + m\alpha, q + n\beta)$. Repeat this for other sets of p and q. There should be $\alpha\beta$ times GSM computations for the layer under consideration.

Step 4) Repeat Step 3) for other layers in the structure. Then combine the individual layer GSM's to find the overall GSM of the structure.

It should be mentioned that in order to increase the computational efficiency and numerical accuracy, the total number

of global Floquet modes must be selected first. This number depends on the element spacings in wavelength and the separation between the adjacent layers [12]. To comply with the total number of global modes requirement, the number of local modes in Step 3) may be considered approximately as $(1/\alpha\beta)$ times the total number of global modes. Therefore, although the GSM's of an individual layer are computed $\alpha\beta$ number of times, the dimensions of the associated matrices are reduced by the same factor.

B. Layers with Different Periodicities and Axes Orientations: Rectangular Lattices

In the foregoing section, the cell orientations between the layers were assumed parallel. In many applications, cell orientations are not parallel between the layers. In this section, we consider rectangular global and local unit cells with nonparallel array axes.

As before, we assume that the global periodicity of the structure is $[a, b]$ and the local periodicity of the ith layer is $[a_i, b_i]$. The x' axis of the ith layer is inclined at an angle ψ with the global x-axis of the structure [see Fig. 2(a)]. The local modal function of the i-th layer can be expressed as

$$\zeta(x, y) = B_{mn} \exp(-jk'_{xm}x' - jk'_{yn}y') \tag{8}$$

where

$$k'_{xm} = (2m\pi + \phi'_{xi})/a_i$$
$$k'_{yn} = (2n\pi + \phi'_{yi})/b_i. \tag{9}$$

Using the following coordinate transformation formulas for axis rotation:

$$x' = x\cos\psi + y\sin\psi$$
$$y' = -x\sin\psi + y\cos\psi \tag{10}$$

and substituting in (8) we obtain

$$\zeta(x, y) = B_{mn} \exp(-jk_{xm}x - jk_{yn}y) \tag{11}$$

with

$$k_{xm} = 2m\pi\cos\psi/a_i - 2n\pi\sin\psi/b_i$$
$$+ \phi'_{xi}\cos\psi/a_i - \phi'_{yi}\sin\psi/b_i \tag{12}$$

$$k_{yn} = 2m\pi\sin\psi/a_i + 2n\pi\cos\psi/b_i$$
$$+ \phi'_{xi}\sin\psi/a_i + \phi'_{yi}\cos\psi/b_i. \tag{13}$$

Recall that a_i and b_i are the periodicities of the ith layer along x' and y' directions, respectively. Now consider the periodicity of the ith layer along x and y directions of the global coordinate system. The periodicity along x would be the l.c.m. of $a_i/\cos\psi$ and $b_i/\sin\psi$[1]. Similarly, the periodicity along y would be the l.c.m. of $a_i/\sin\psi$ and $b_i/\cos\psi$. Since $[a, b]$ is the global periodicity the following relations must hold:

$$a = m_1 a_i/\cos\psi = n_1 b_i/\sin\psi$$

[1]For all practical purposes $a_i/\cos\psi$ and $b_i/\sin\psi$ can be considered as rational numbers, hence an l.c.m. is possible to obtain.

$$b = m_2 a_i / \sin \psi = n_2 b_i / \cos \psi \qquad (14)$$

where m_1, m_2, n_1, n_2 are all integers. Using (14) in (12) and (13) we obtain

$$k_{xm} = [2\pi(mm_1 - nn_1) + (m_1\phi'_{xi} - n_1\phi'_{yi})]/a$$
$$k_{yn} = [2\pi(mm_2 + nn_2) + (m_2\phi'_{xi} + n_2\phi'_{yi})]/b. \quad (15)$$

Suppose the above wave number corresponds to the (p, q) global mode with a differential-phase pair $\{\phi_x, \phi_y\}$. Then, we can write

$$2\pi p + \phi_x = 2\pi(mm_1 - nn_1) + (m_1\phi'_{xi} - n_1\phi'_{yi})$$
$$2\pi q + \phi_y = 2\pi(mm_2 + nn_2) + (m_2\phi'_{xi} + n_2\phi'_{yi}). \quad (16)$$

Equation (16) essentially relates the local mode indexes (m, n) to the global modal indexes (p, q). For given ϕ_x and ϕ_y (which are determined from desired scan direction or from other considerations), each global mode-index pair has a corresponding local mode-index pair and vice versa. In other words, every local mode, represented by a coordinate point on the $(m - n)$ plane, has an image point on the $(p - q)$ plane [see Fig. 2(b) and (c)]. Since m and n can take all possible integer values, a unit cell in the $(m - n)$ plane, in general, maps into a parallelogram in $(p - q)$ plane as shown in Fig. 2(c). The area of the parallelogram can be found from the Jacobian relation of (16), which is given by

$$\Delta p \Delta q = \frac{\partial(p, q)}{\partial(m, n)} \Delta m \Delta n. \qquad (17a)$$

From (16) and (17) we obtain

$$\Delta p \Delta q = m_1 n_2 + m_2 n_1 = ab/(a_i b_i) \qquad (17b)$$

since $\Delta m = \Delta n = 1$. The number of discrete coordinate points inside the parallelogram is equal to $m_1 n_2 + m_2 n_1 = ab/a_i b_i$, which is expected. If we excite the ith layer with a differential-phase pair $\{\phi'_{xi}, \phi'_{yi}\}$ that satisfies (16), then the global modes will occur at discrete intervals. Each differential-phase pair associates only one global mode point within each parallelogram. The remaining mode points correspond to other differential-phase pairs. To generate the other global modes we should use appropriate sets of $\{\phi'_{xi}, \phi'_{yi}\}$. The procedure of finding appropriate $\{\phi'_{xi}, \phi'_{yi}\}$'s will be explained shortly. To fill in the entire global modal space, one can follow a systematic procedure as below:

Step 1) Estimate the global cell size $[a, b]$ and the global coordinate axes for the structure. Consider the ith layer. Use (14) to find m_1, n_1, m_2 and n_2, which depends on $[a_i, b_i]$, $[a, b]$, and ψ. Find ϕ_x and ϕ_y from the excitation condition of the array or other conditions relevant to the function of the structure.

Step 2) Construct a parallelogram in the $(p - q)$ plane. The four corner points of the parallelogram are $(0, 0)$, (m_1, m_2), $(-n_1, n_2)$ and $(m_1 - n_1, m_2 + n_2)$, respectively. Locate all the discrete points (with integer coordinates) inside the parallelogram.
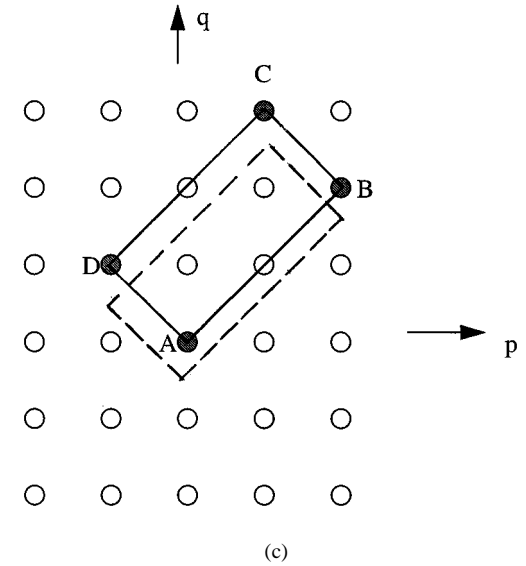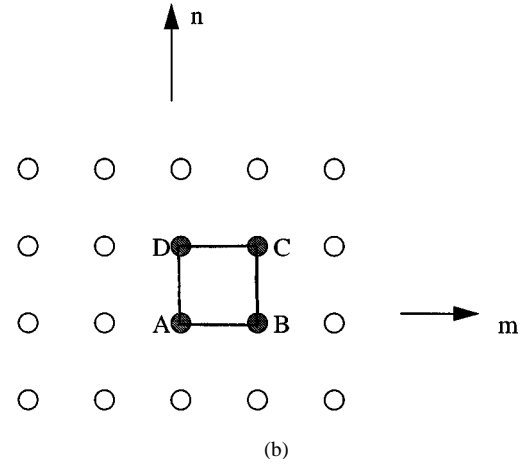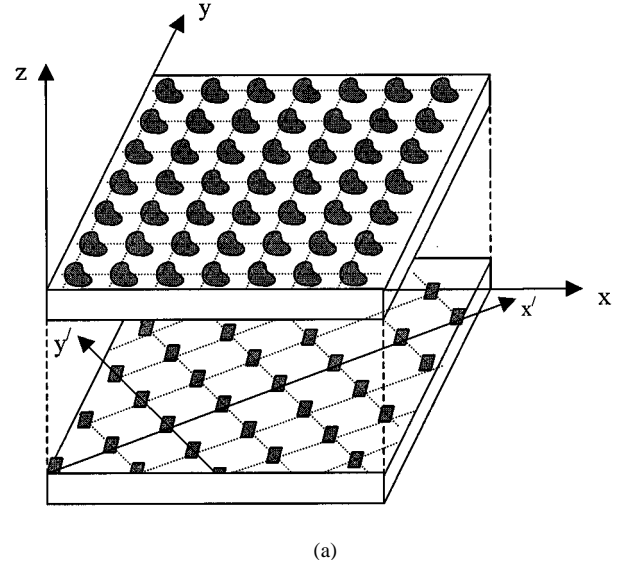

Fig. 2. (a) Two-layered printed array structure (rectangular lattices) with different periodicities and non-parallel array axes orientations. (b) Floquet local mode-index $(m - n)$ plane. (c) Floquet global mode-index $(p - q)$ plane.

Step 3)

a) Set $m = n = p = q = 0$. Then use (16) to obtain ϕ'_{xi} and ϕ'_{yi}. Obtain the local GSM

of the ith layer for a differential-phase pair $\{\phi'_{xi}, \phi'_{yi}\}$. Rename all the (m, n) modal indexes of the local GSM elements by (p, q), where p and q are computed using (16). Note that (p, q) occurs at discrete intervals only.

  b) Select another discrete point inside the parallelogram of Step 2) and find (p, q). Set

$$p = mm_1 - nn_1$$
$$q = mm_2 + nn_2 \qquad (18)$$

and find solutions for m and n. At least one of them (m or n) must be noninteger. Retain only the integral parts as the solutions for m and n. Use the integral values thus obtained for m and n in (16) to find a new set of ϕ'_{xi} and ϕ'_{yi}. With this new $\{\phi'_{xi}, \phi'_{yi}\}$ repeat Step 3a). If some points lie on the boundary of the parallelogram, shift the parallelogram in appropriate directions (no rotation allowed) so that no point lies on the boundary. Then consider all the points inside the shifted parallelogram [parallelogram with dash lines in Fig. 2(c)].

Step 4) Repeat Step 3b) for other discrete points inside the parallelogram. There should be a total of $m_1 n_2 + m_2 n_1$ local GSM computations for the ith layer.

Step 5) Follow Steps 1) to 4) for the other layers and cascade the global GSM's to obtain the overall GSM of the structure.

The procedure presented above is applicable for rectangular lattice structures. For other lattice structures or for different lattices at different layers (for example, rectangular in one layer and triangular in other layer) the mapping relations would be different. This is considered in the section that follows.

C. Layers with Different Periodicities and Different Axes Orientations: Arbitrary Lattices

The procedure in Section II-B can be generalized for different lattice structures at different layers. A general lattice structure of the ith layer is shown in Fig. 3. The unit cell area is $a_i \times b_i$ where a_i is the element spacing along the row (x'-axis), b_i is the perpendicular distance between two consecutive rows and γ_i is the lattice angle. The three parameters a_i, b_i and γ_i can describe any arbitrary unit cell. Different unit cell structures at different layers may result in a general global unit cell structure. Suppose the global unit cell has a lattice angle γ and the cell area is $a \times b$ (Fig. 3). The row-axis (x-axis) of the global cell makes an angle ψ with the x'-axis of the local cells. The local wave numbers associated with the (m, n) local mode in the ith layer can be expressed as

$$k'_{xm} = (2m\pi + \phi'_{xi})/a_i$$
$$k'_{yn} = (2n\pi + \phi'_{yi})/b_i - 2m\pi/(a_i \tan\gamma_i). \qquad (19a)$$

We like to mention that although the wave number along y is a function of both m and n, for simplicity we keep the same
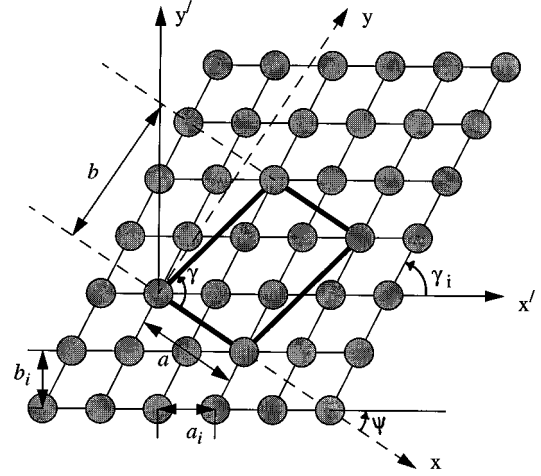

Fig. 3. Arbitrary lattice structure of a layer. Also shown are the global unit cell (thick-line parallelogram) and the relative axis orientation. $a \times b$ is the area of a global unit cell; $a_i \times b_i$ is the area of a local unit cell.

notation as in the case of a rectangular lattice. The global wave numbers corresponding to the (p, q) global mode are

$$k_{xp} = (2p\pi + \phi_x)/a$$
$$k_{yq} = (2q\pi + \phi_y)/b - 2p\pi/(a \tan\gamma). \qquad (19b)$$

Following the procedure detailed in Section II-B, we can find the relation between the local and the global mode indexes. The final relation becomes

$$2\pi p + \phi_x = 2\pi(mm_1 - nn_1) + (\alpha_1\phi'_{xi} + \beta_1\phi'_{yi})$$
$$2\pi q + \phi_y + b\phi_x/(a \tan\gamma) = 2\pi(mm_2 + nn_2) + (\alpha_2\phi'_{xi} + \beta_2\phi'_{yi}) \qquad (19c)$$

where

$$\alpha_1 = a\cos\psi/a_i, \quad \beta_1 = -a\sin\psi/b_i$$
$$\alpha_2 = b\cos(\gamma - \psi)/(a_i \sin\gamma)$$
$$\beta_2 = b\sin(\gamma - \psi)/(b_i \sin\gamma).$$

m_1, n_1, m_2, n_2 are four integers and their values are $a\sin(\psi + \gamma_i)/(a_i \sin\gamma_i)$, $a\sin\psi/b_i$, $b\sin(\psi + \gamma_i - \gamma)/(a_i \sin\gamma \sin\gamma_i)$, and $b\sin(\gamma - \psi)/(b_i \sin\gamma)$, respectively. To obtain the global GSM from local GSM's of the ith layer one should use (19c) instead of (16) and then follow the steps from 1 through 4 in Section II-B. Notice that setting $\gamma_i = \gamma = 90°$, (19c) modifies to (16).

III. APPLICATIONS

To demonstrate the methodology, we consider the following three examples of practical importance. In order to validate the theory, we compare our computed results with the available results in the literature.

A. Patch-Fed Patch Subarray

A patch fed patch subarray is considered as the first example of a multilayer (two layers in this case) array structure with different periodicities. Fig. 4(a) shows the geometry of a unit
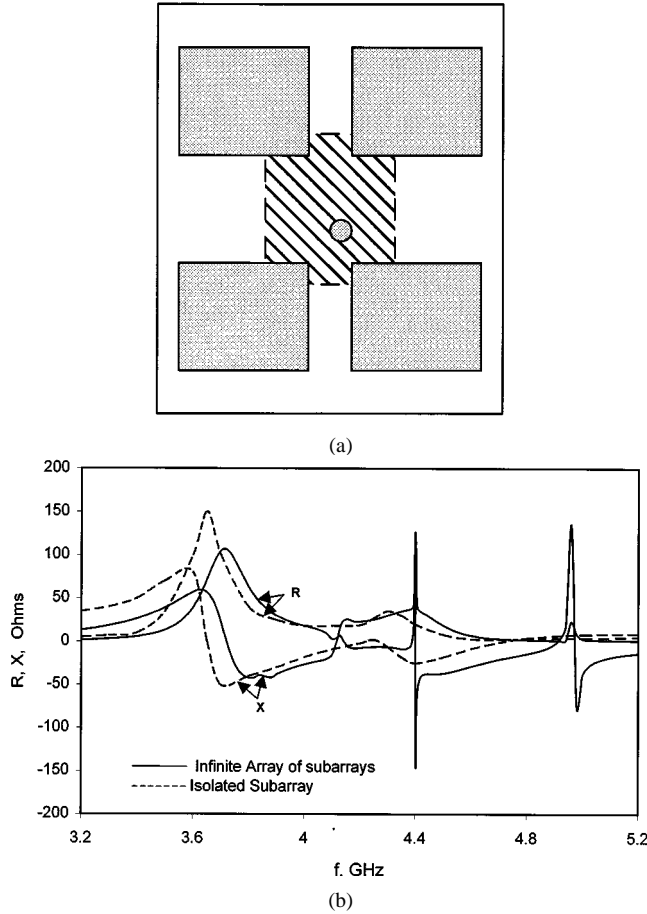
(a)

(b)

Fig. 4. (a) A two-layered patch-fed patch subarray. The lower layer patch electromagnetically couples the upper layer patches. Lower layer patch is excited by probe feed. (b) Input impedance versus frequency plot of the subarray. Subarray E-plane dimension $= 7.2$ cm, H-plane $= 6.4$ cm, upper layer patches 2.0 cm $\times$ 1.6 cm, lower layer patch 2.13 cm $\times$ 2.0 cm. Substrate thickness of the layers $= 0.16$ cm each, dielectric constant for both layers $= 2.55$. Probe located at 0.8 cm from the center along E-plane. — Infinite array of subarrays for bore-sight radiation; --- isolated subarray [6].

cell of the structure. The array consists of two patch layers on a dielectric coated ground plane. Another dielectric layer separates the patch layers. Probes excite the lower layer patches. Each lower layer patch electromagnetically couples four upper layer patches. The driven patch in the lower layer and the four coupled patches in the upper layer make a subarray of an infinite array. The lower layer patches have the periodicity $[a, b]$, while the upper layer patches have the periodicity $[a/2, b/2]$. Both layers have rectangular lattice structures. In a global unit cell, the driven patch is symmetrically located below four upper layer patches. Analysis of an isolated subarray is reported by Legay and Shafai [6]. However, our analysis is applicable for infinite array of such subarrays.

To analyze the infinite array, we first find the local GSM's of the upper layer and convert the local GSM's to a global GSM using the steps in Section II-A. For the upper layer, we compute four local GSM's with differential-phase pairs $\{\phi_x/2, \phi_y/2\}$, $\{\phi_x/2 + \pi, \phi_y/2\}$, $\{\phi_x/2, \phi_y/2 + \pi\}$, $\{\phi_x/2 + \pi, \phi_y/2 + \pi\}$, respectively, where $\phi_x = k_0 a \sin\theta \cos\phi$, $\phi_y = k_0 b \sin\theta \sin\phi$, (θ, ϕ) being the scan direction in the spherical coordinate system. We consider $[a/2, b/2]$ as the local cell size for the

upper layer. The local mode indexes are then converted to obtain the global GSM for the upper layer. Because the cell centers between the two layers are misaligned, appropriate phase factor is introduced for each elements of the global GSM. To compute the GSM of the lower layer, we use $\{\phi_x, \phi_y\}$ as the differential-phase pair and $[a, b]$ as the cell size. The two global GSM's are combined to obtain the overall GSM of the patch layers. To find the input impedance seen by the probe feed, the overall GSM is converted to the $[Z]$ matrix. The $[Z]$ matrix of the probe feed is obtained separately using the reaction theorem and Floquet modal analysis [13]. Combining the $[Z]$ matrices, the input impedance seen by the probe is obtained.

In Fig. 4(b) we have plotted the input impedance. About 120 Floquet modes were used to obtain a reasonable convergence. To compare the impedances between an isolated subarray and its infinite array, we have also plotted the input impedance of an isolated subarray. The impedance data were extracted from Fig. 2 of [6]. High Q resonances are found to occur for the infinite array case. For the isolated subarray, no such resonance exists. The high Q resonances near 4.4 and 5 GHz are due to the parallel plate modes that couple with higher order Floquet modes. The uncharacteristic behavior of the array impedance near 4.16 GHz is due to the appearance of the first grating lobe. If the high Q resonance points are ignored (which are pertinent to an infinite array), the general shapes (including the number of peaks) of the impedance curves are very similar to each other.

B. Array of Subarrays

For a limited scan requirement, the subarray concept is useful, because it allows lesser number of phase shifters than normal. To excite the subarray elements with appropriate tapering, which is sometimes necessary to control the grating lobes [14], one should have a knowledge of the impedance matrix of the subarray elements. The usual way of analysis is to consider the entire subarray as a unit cell of the array and then solve the patch currents using the method of moments [15]. This method requires excessive analytical and computational efforts because all patch currents in a subarray are solved simultaneously with a large number of unknowns. Furthermore, the cell size being larger, several Floquet modes are required for a reasonable convergence. In the present approach, we use the general procedure outlined in Section II with necessary modifications for $[Z]$ matrix representation of a subarray. We will demonstrate that one needs to characterize only one element in a subarray to characterize the entire subarray consisting of several identical elements. To simplify the presentation we outline the procedure for a rectangular subarray of 2×2 elements as in Fig. 5(a). In the Appendix, we consider more general subarrays with arbitrary number of elements.

Suppose $[a, b]$ are the dimensions of a subarray (rectangular lattice) in an infinite array. As explained in Section II-A, we consider the local cell size as the element spacing inside a subarray. The cell size in this case is $[a/2, b/2]$. Now we compute the Floquet impedances of the array elements with the following differential phase pairs: $\{\phi_x/2, \phi_y/2\}$, $\{\phi_x/2 + \pi, \phi_y/2\}$, $\{\phi_x/2, \phi_y/2 + \pi\}$, $\{\phi_x/2 + \pi, \phi_y/2 + \pi\}$, where $\phi_x = k_0 a \sin\theta \cos\phi$, $\phi_y = k_0 b \sin\theta \sin\phi$, (θ, ϕ)
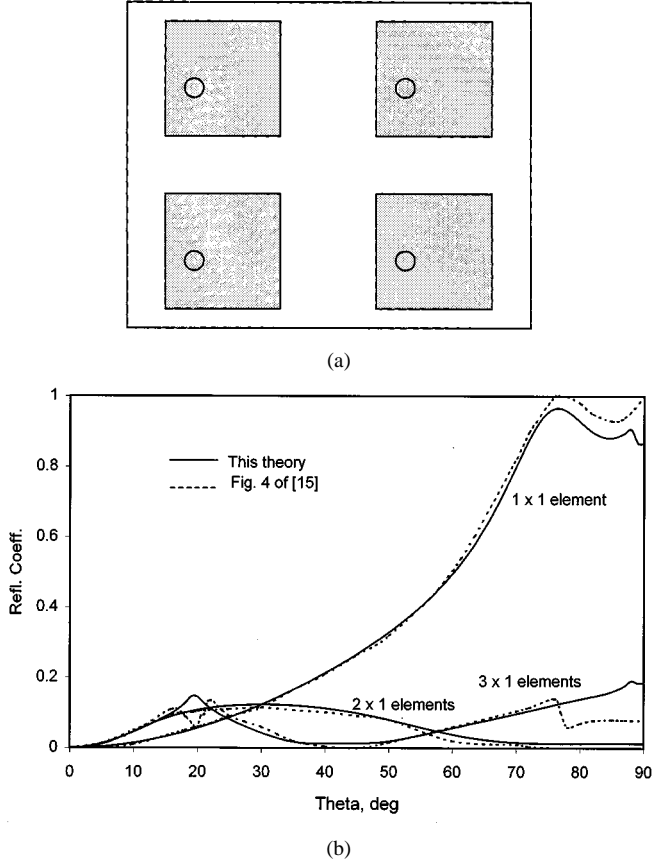
(a)

(b)

Fig. 5. (a) Subarray of 2×2 patch elements. (b) Reflection coefficient versus E-plane scan angle of an infinite array of subarrays. Number of elements in subarrays are 1×1, 2×1, and 3×1, respectively. Subarray elements are arranged along the E-plane. Element spacing within a subarray $0.5\lambda \times 0.5\lambda$. Element size $0.28\lambda \times 0.3\lambda$. Dielectric constant $= 2.55$. Equal voltages for all the elements within a subarray. —This theory; --- [15].

being the scan angle. Suppose Z_{1F}, Z_{2F}, Z_{3F} and Z_{4F} are the Floquet impedances for the above four cases. Then the impedance matrix of the subarray elements for a given scan angle would be (see Appendix for derivation)

$$[Z] = [\Phi][Z_F][\Phi]^{-1} \qquad (20)$$

where $[Z_F]$ is a diagonal matrix, $Z_{1F}, Z_{2F}, Z_{3F}, Z_{4F}$ being the diagonal elements, and $[\Phi]$ is given by

$$[\Phi] = \begin{bmatrix} 1 & 1 & 1 & 1 \\ x & -x & x & -x \\ y & y & -y & -y \\ xy & -xy & -xy & xy \end{bmatrix} \qquad (21)$$

with

$$x = \exp(j\phi_x/2)$$
$$y = \exp(j\phi_y/2).$$

Note that $[\Phi]$ is an orthogonal matrix that can be inverted by transposing its complex conjugate and then multiplying with the normalization constant. If the number of elements in a subarray increases indefinitely, the mutual impedance between the elements approaches the integral relation derived in [16].
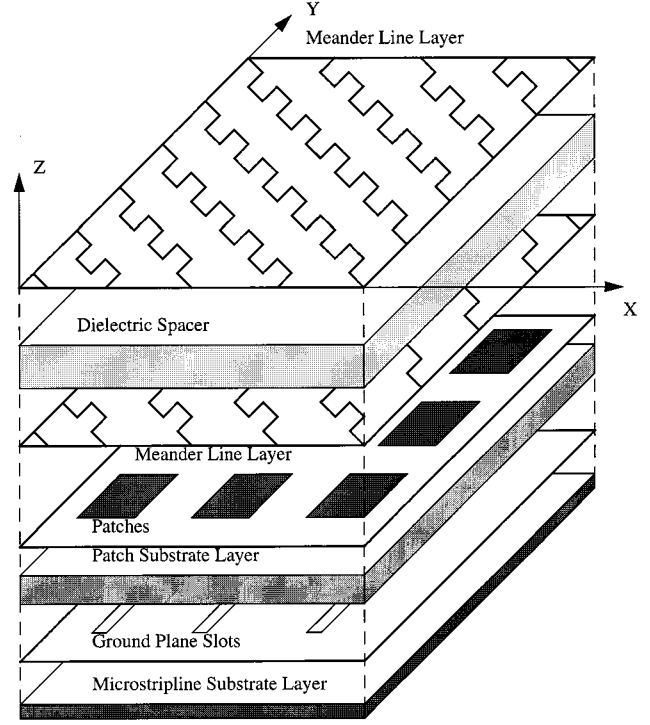

Fig. 6. Exploded view of a slot-coupled patch array loaded by a meander-line polarizing screen for circular polarization.

In order to validate the above subarray analysis, we compute the impedance matrix of three subarrays with elements 1×1, 2×1, and 3×1, respectively. From the impedance matrix, the active input impedances seen by the patch elements of a subarray are obtained. From the active impedances, we derive the reflection coefficient seen by an equal-split power divider. Each subarray is assumed to be boresight matched. We compute the reflection coefficients for several scan angles in the E-plane and compare our numerical results with that reported in [15]. Fig. 5(b) shows the comparison. For our numerical results, we assume that the feed probes are located near the radiating edges of the patch elements. Excellent agreements between the two sets of results are found. For 3×1 element subarray, discrepancies are found near $\theta = 20°$ and $\theta = 75°$ scan angles. These two angles correspond to the array blind spots. The magnitude of the reflection coefficient near the blind spot is very sensitive to the feed location. We assume the feed location near the edge of the patch elements, which may be different from that in [15].

C. Patch Array Loaded with Screen Polarizer

We now present an example of a multilayer structure with different periodicities and array-axes orientations. An exploded view of the entire structure is shown in Fig. 6. It is a slot-fed patch array antenna loaded with a two-layered polarizing screen. The patch array is designed to radiate linearly polarized wave with its polarization direction along the x-axis. The screen polarizer converts the fields from linear polarization to circular polarization. The screen polarizer consists of a dielectric layer with conducting meander-lines (or strip-lines) etched on both sides of the layer. The screen polarizer is placed above the patch surface
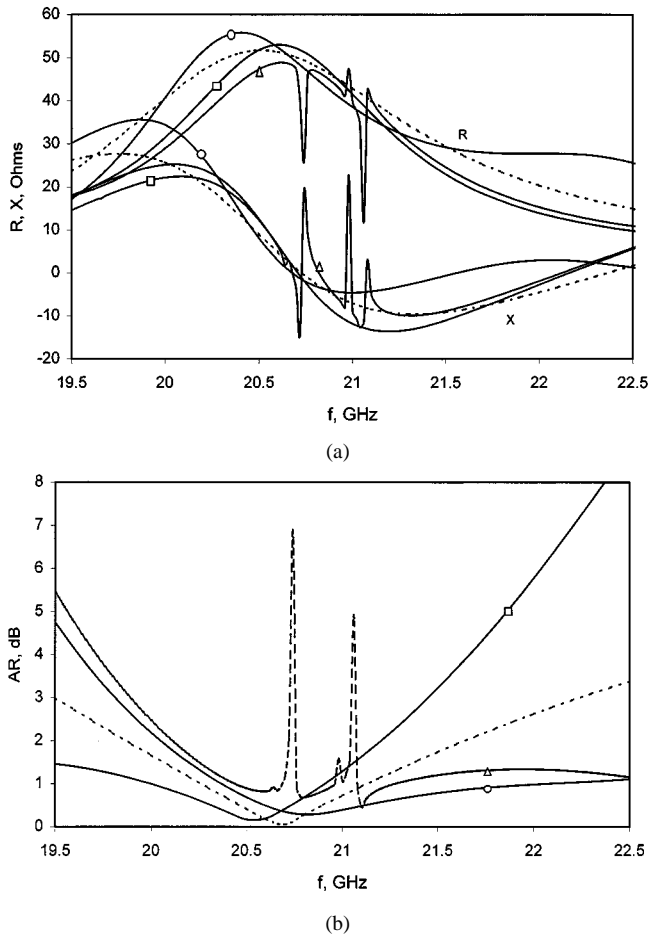

(a)

(b)

Fig. 7. Impedance and axial ratio of the structure in Fig. 6. Patch cell size 0.99 cm × 0.99 cm. Patch size = 0.35 cm × 0.6 cm. Slot size = 0.27 cm × 0.025 cm. Patch substrate thickness = 0.081 cm, feed substrate thickness = 0.038 cm. Dielectric constant for patch substrate (also feed substrate) is 2.55. 50 Ω microstrip feed lines excite slots. Meander-line periodicity 0.7 cm × 0.35 cm. Line width = 0.035 cm, meander depth = 0.1 cm. Meander-line axis is $135°$ with x-axis of patch array. Polarizer spacer thickness = 0.502 cm, dielectric constant of spacer = 1.1. Strip-width for the strip-line polarizer = 0.025 cm, spacer thickness = 0.5 cm. (a) Input impedance versus frequency. --- patch array without polarizer, -△- patch array with strip-line polarizer at $d = 0.5$ cm, -□- patch array with meander-line polarizer at $d = 0.5$ cm, -O- patch array with meander-line polarizer at $d = 0.7$ cm, d = distance between the patch surface and polarizer inner surface. (b) Axial Ratio versus frequency. --- meander-line polarizer by itself for normal plane wave incidence, -△- patch array with strip-line polarizer at $d = 0.5$ cm, -□- patch array with meander-line polarizer at $d = 0.5$ cm, -O- patch array with meander-line polarizer at $d = 0.7$ cm.

and at a finite distance from the patch metallization. The distance between the patch and the polarizer is adjusted to optimize the electrical performance of the antenna. Analysis of an isolated screen polarizer has been reported in the literature [9]. We will present a detailed analysis of the patch-polarizer assembly. We shall see shortly that the scan performance of an isolated screen polarizer differs considerably from that when coupled to a patch array.

In our structure, the periodicity of the patch elements is 0.99 cm in both directions. For the screen polarizer, the spacing between two grid lines is 0.35 cm and the grids are oriented at an angle $135°$ with the E-plane of the patch array. The meander periodicity along the length is 0.7 cm. The x'-axis of the meander-line makes $45°$ angle with the x-axis of the patch. Using
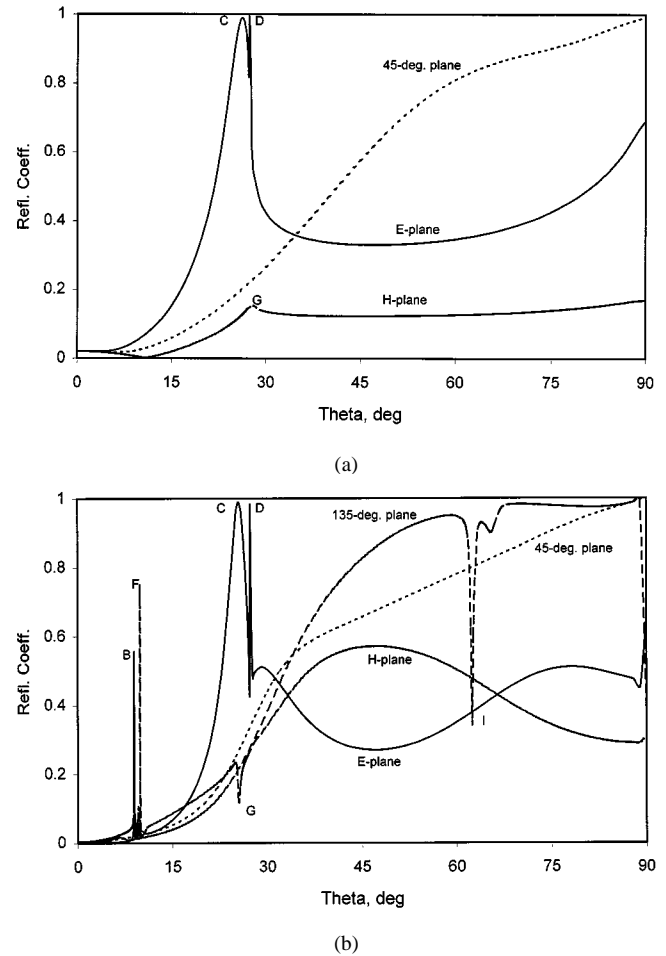

(a)

(b)

Fig. 8. (a) Reflection coefficient versus scan angle of the slot-coupled patch array (no polarizer) described in Fig. 7. (b) Reflection coefficient of the patch array with meander-line polarizer loading. Separation between patch surface and the inner surface of the polarizer is 0.5 cm. $f = 20.7$ GHz. The resonances are explained through circle diagram in Fig. 9.

(14) we find $m_1 = m_2 = 2$ and $n_1 = n_2 = 1$. Following the steps in Section II, we find the GSM of the structure with respect to the global modes. From the GSM, we determine the input impedance, axial ratio of the array. Fig. 7(a) shows the input impedance of an element with and without screen polarizers. Two different polarizers (meander-line and strip-line polarizers) are considered for this study. The impedances are computed for boresight beams. The polarizers reduce the impedance bandwidth of the array. The strip-line polarizer introduces high Q resonances, which are due to coupling between strip-line modes and higher order Floquet modes. For meander-line polarizer no such resonance occurs for the boresight beam. We will explain these phenomena later in further details. Fig. 7(b) shows the axial ratio versus frequency for three different screen locations. By adjusting the spacing between patch surface and the screen polarizer, the array structure can be tuned to some extent to improve the axial ratio of the radiated fields. For the strip-line polarizer, the axial ratio degrades significantly at the resonance locations.

To examine the scan performance of the integrated array structure, we compute the reflection coefficient seen by the microstrip feed line at various scan planes. Fig. 8(a) and (b)

shows the scan performance of the patch array without and with meander-line polarizer loading. The scan planes were $0°$, $45°$, $90°$, and $135°$, respectively. Several blind spots are found. These blind spots are due to the trapped guided modes that exist between the polarizer screen and the patch ground plane. There are three different types of guided modes responsible for scan blindness. They are: 1) surface wave modes; 2) meander-line-guided modes; and 3) parallel—plate waveguide modes. The occurrence of a scan blind angle can be explained through the Floquet mode circle diagram in Fig. 9. Each circle (with radius equal to k_0) is associated with a Floquet mode supported by the array structure. The family of curves (almost straight lines with small periodic perturbations) in the diagram represent the wave number loci of meander-line-guided modes[2]

The meander mode loci were obtained from an independent analysis of meander-line structure over a ground plane. The loci are oriented at $45°$ with the k_x-axis, because the meander-line axis is at $135°$ with the x-axis of the patch array (Fig. 6).

In Fig. 9, the circle with slightly larger radius, concentric with the $(0,0)$ mode represents the surface wave mode. Whenever a guided mode locus passes through a Floquet mode circle, it indicates that the Floquet mode and the guided mode may be strongly coupled to each other, causing a resonance that may lead to a scan blindness. Each point of the guided mode locus that lies inside the Floquet mode circle corresponds to a blind spot. For example, the point B represents a blind spot due to coupling between a meander-line mode and the $(-1,0)$ Floquet mode. The blind spot is represented by the vector $\vec{AB}$, so the blind spot is located at $\phi = 0$ (E-plane), $\theta = \sin^{-1}(|AB|) \approx 9°$. Likewise, the vector $\vec{AC}$ represents the scan blindness on the E-plane due to the surface wave resonance. Similarly, the vector $\vec{HI}$ represents a blind spot at $\phi = 135°$ and $\theta \approx 63°$. In Fig. 9, we have shown the points corresponding to each blind angle of Fig. 8(b). Note that some of the above blind spots would not be observed in the case of an isolated meander-line polarizer with a plane wave incidence, because those blind spots are due to coupling between higher order Floquet modes and the meander-line-guided modes.

It is important to note that the meander-line polarizer introduces undesirable blind spots at about $9°$ angle from the boresight direction of the array. The intensity of the above blindness can be reduced or eliminated if the coupling between the meander mode and the Floquet mode associated with the blind spot is reduced. This can be accomplished if the distance between the meander-line polarizer and the patch surface is increased, because the coupling Floquet mode is evanescent, so the fields decay exponentially along z. In Fig. 10 we have shown the scan performance of the same antenna structure, when the polarizing screen position is elevated by 0.5 cm along z. Notice that the meander mode resonance is completely subsided, enhancing the scanning range of the array. However, by elevating the screen position, we find few additional peaks (resonances)

[2]If β be the propagation constant of a guided mode, then the guided mode will be coupled to any Floquet mode that has a wave number of $(2n\pi/b \pm \beta)$, where b represents the periodicity of the Floquet mode along the meander-line-mode propagation direction and n is an integer. Therefore, to examine he coupling between all possible Floquet modes and the meander-line mode we should plot two sets of loci—one being the mirror image of the other—as shown in Fig. 9.
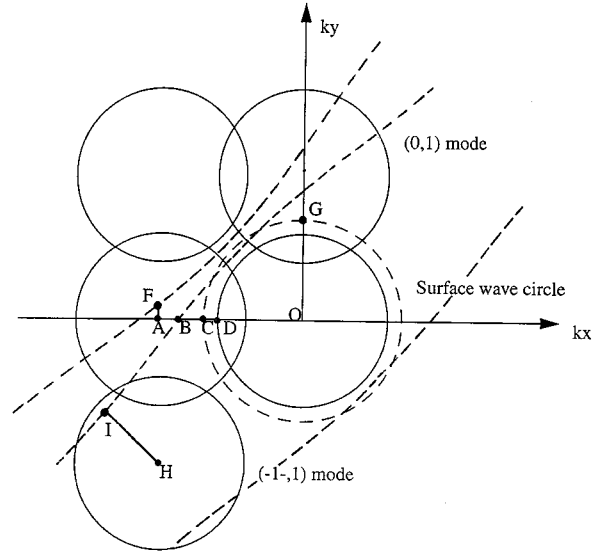

Fig. 9. Floquet mode circle diagram. Each circle corresponds to a Floquet mode. The circle with dash lines corresponds to the TM_0 surface wave mode. The family of curves represents the propagation constant loci of the meander-line-guided modes. The points indicated by capital letters correspond to the resonances in Fig. 8(a) and (b).
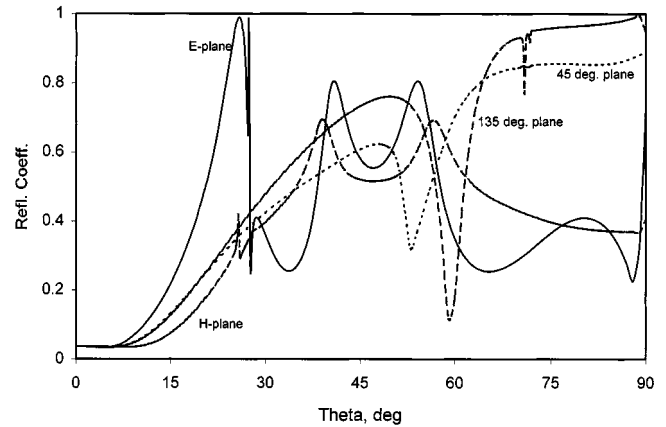

Fig. 10. Scan performance with elevated ($d = 1.0$ cm) meander-line polarizing screen. The other parameters are same as that in Fig. 7.

in the reflection curves. These peaks correspond to the parallel plate waveguide modes that propagate along the transverse direction with multiple reflections from two reflecting planes. The incident angle of the wave front is given by

$$\theta = \cos^{-1}(n\lambda/2d) \qquad (22)$$

where n is an integer, λ is the wavelength inside the parallel plate region and d is the distance between the two planes. Since the upper plane is made of meander-lines, the location of the upper reflection plane slightly deviates from the physical location of the meander-line plane. This deviation depends on the incident angle and polarization angle of the incident field. To estimate the location of resonance, we wave plotted the distance of apparent plane of reflection versus the scan angle in Fig. 11.

The distance of apparent plane of reflection is estimated using the following expression:

$$d = d_1 + \delta z \qquad (23)$$

where d_1 is the equivalent "free-space distance" (considering two different dielectric media) between the inner plane of the polarizer and the patch ground plane and δz is the distance of the apparent plane of reflection in the vicinity of the polarizer inner surface. δz is obtained from the following relation:

$$B = -1/\tan(k_0 \delta z \cos\theta) \qquad (24)$$

where B is the input susceptance of the polarizer with respect to either the TE$(0,0)$ or the TM$(0,0)$ mode incidence that has a larger reflection coefficient. θ is the scan angle and k_0 is the free-space wave number. Resonance occurs when the distance between the two planes of reflections satisfies (22). To find the resonance points we have also plotted the function $\lambda/(2\cos\theta)$ versus θ in Fig. 11. The intersection points correspond to resonances. The intersection points are found at $\theta = 56°$ for the E- and H-planes, $\theta = 55°$ for $\phi = 45°$ plane, and $\theta = 59°$ for $\phi = 135°$ plane. These resonant locations closely agree with that observed in Fig. 10. These simple relations give an estimate of the resonant locations, however for an accurate prediction one has to analyze rigorously as has been done for Fig. 10.

It can be noted in Fig. 10 that for the $\phi = 0°$ and $\phi = 90°$ cuts resonances occur near $\theta = 40°$. These resonances are due to the $(1,0)$ and $(0,1)$ modes, respectively, that also couple to the parallel plate modes. From grating-lobe point of view, when the array scans at $\theta = 41°$ on the E-plane, the grating lobe appears at $\theta = 54°$ and vice versa, causing resonances at both $41°$ and $54°$ scan locations on E-plane. For $45°$ and $135°$ planes the grating lobes do not exist, therefore, only one parallel-plate mode resonance occurs in each of these scan planes.

To compare the scan performance between a meander-line polarizer and a strip-line polarizer, we present the scan characteristics of a patch array loaded with a strip-line polarizer in Fig. 12. We notice that the nearest blind spot occurs at about $1°$ scan angle for the E- and H-plane scans, as opposed to the $9°$ for the meander-line case [see Fig. 8(b)]. This effect can be explained from the circle diagram presented in Fig. 9. For the strip-line polarizer, the loci for the strip-line guided mode would be almost a straight line with $45°$ angle of inclination with the k_x axis (as compared to somewhat zigzag line for meander-line-guided mode). Therefore, one of the loci will intersect the k_x axis at a point very close to the $(-1,0)$ mode circle's center. In other words, the magnitude of the $\vec{AB}$ vector will be smaller in this case, as compared to that of the meander-line polarizer, resulting in a smaller blind angle. Similar argument applies to the H-plane scan. It is worth mentioning that by adjusting the patch cell size, we can move the center of the higher order Floquet mode circles. Consequently, some of the blind spots will move from their previous locations.

Another important difference between a strip-line polarizer and a meander-line polarizer is observed in the $45°$ scan plane. The strip-line polarizer shows several resonances whereas
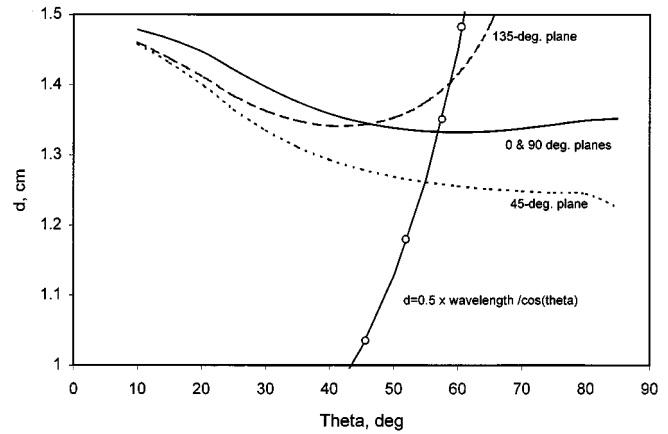

Fig. 11.   Apparent plane of reflection of a meander-line surface versus scan angle. The stiff curve is $\lambda/(2\cos\theta)$ versus θ. The intersection points represent blind spots caused by parallel plate modes.
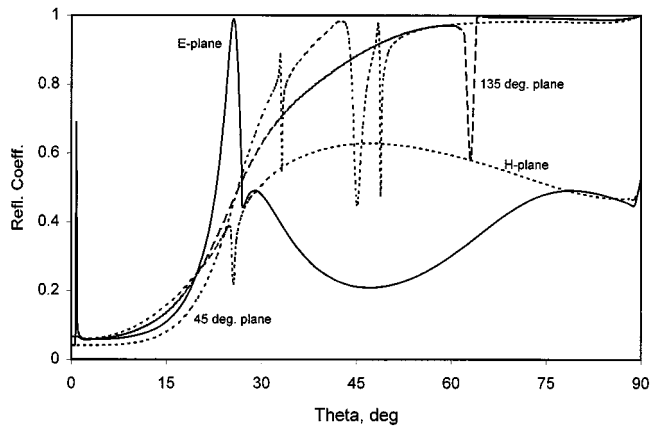

Fig. 12.   Scan performance of the patch array of Fig. 7 when loaded with the strip-line polarizer. Separation between patch surface and polarizer is 0.5 cm. strip-line polarizer dimensions are given in Fig. 7.

the meander-line polarizer shows only one resonance. The resonance near the $33°$ angle is due to a parallel plate mode that propagates between the ground plane and the lower strip-grid layer. High inductive reactance of the strips moves the apparent plane of reflection above the strip-grid surface, which effectively lowers the cutoff frequency, facilitating the parallel plate mode to propagate. From the analysis, it is found that, this parallel plate mode couples with the $(-1,0)$ Floquet mode, which is evanescent. Therefore, elevating the polarizer screen can eliminate this resonance. The resonances near $45°$ and $48°$ angles are due to other higher order parallel plate modes. One of the modes propagates between the upper grid layer and the patch ground plane and the other propagates between the upper grid layer and the patch surface layer. The above two scan angles closely match with the formula in (22), if d is considered as the distance between the upper grid layer and the patch ground plane or the patch surface layer. It is also found that if the separation between the patch layer and the polarizer increases, the resonances move to larger angles, which also comply with (22). These two resonances are due to the coupling between the $(0,0)$ Floquet mode and higher order parallel plate modes. Therefore, unlike the resonance discussed

before (at 33°), elevating the polarizer screen does not eliminate these resonances; moves the resonant locations only.

It is interesting to note that if the polarizer grids are parallel to the H-plane of the patch array, the additional scan blindness (besides the blindness due to the surface wave modes) in the E-plane due to polarizer loading may not occur. For such configurations the strip-line-mode loci generally do not intersect with the k_x axes of the Floquet mode circles, hence the Floquet modes and the strip-line modes do not couple to each other. This observation is in conformity with that reported in [11]. For large element spacing in the H-plane, however, a strip-line mode locus may intersect with the k_x axis at a point inside a Floquet mode circle and scan blindness may occur in the E-plane. Similar argument applies to E-plane parallel grids. However, these situations do not arise in the case of circular polarizer screens, because for circular polarization, the grid axis must not be parallel with the E or H-plane of the patch array.

In order to examine the validity of the analysis we present the measured return loss of a Ka-band subarray of 4×4 patch elements loaded with a two-layer strip-line polarizer. The periodicity of the patch elements was 0.876 cm $\times$ 0.876 cm. The polarizer grids were spaced at 0.35 cm and the grids were oriented at 45° angle with respect to the patch axis. The polarizer screen was placed at 0.22 cm above the patch surface. The patches within a subarray were excited by a $1:16$ binary split power divider (with several Tee-junctions and quarter wave transformers) realized in asymmetric striplines. The patch elements were coupled with the striplines through ground plane slots. To suppress the parallel plate modes, each slot was surrounded by eight plated-through vias. The measurement was conducted in a large array environment where the other subarrays were matched terminated. Fig. 13 shows the computed and measured return loss seen at the input end of the power divider of a subarray. The agreement between the two results is good. The array was designed to operate between 20.2 and 21.2 GHz. Computed return loss is -15 dB or better within the band. The slight discrepancy between the two curves is attributed to fabrication tolerances and uncertainty in the dielectric constant values.

IV. CONCLUSION

We presented a general analysis of multilayer structure where the layers may have different lattice structures, cell sizes, and array axis orientations. Each layer is analyzed locally using Floquet modal expansion and GSM approach. The local GSM's are then converted to a global GSM associated with a global coordinate system and the global unit cell structure. All individual layer global GSM's are cascaded to characterize a multilayered structure. The methodology has the following advantages.

- It is a modular approach, layers are analyzed independently (easy to handle a multilayer structure).
- The method is numerically more efficient as compared to a "brute-force" approach, where a global cell is considered as a unit cell and the currents in all the elements in a unit
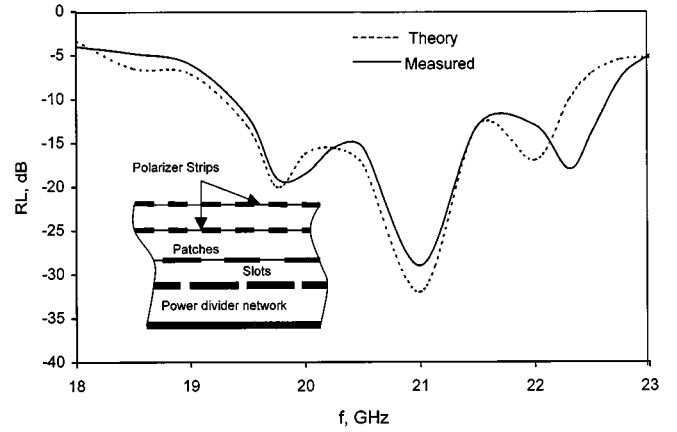

Fig. 13. Computed and measured return loss of a 4×4 slot-fed patch subarray loaded with a two-layer strip-line polarizer screen. Patch substrate thickness = 0.091 cm, dielectric constant = 2.56. Polarizer is at 0.22 cm above the patch surface. Polarizer grid spacing = 0.35 cm. Polarizer thickness = 0.496 cm. ---- computed; — measured.

cell are solved simultaneously with increasing number of unknowns.
- A lesser number of modes can be used to obtain the local GSM's, because individual layers have smaller cell dimensions than the global cell.

The patch array structure, loaded with a polarizer screen exhibits several interesting characteristics. Some of them are outlined below.

- Electrical performance (especially the axial ratio) can be tuned by adjusting the distance between the patch layer and the polarizer layer.
- Both meander-line polarizer and strip-line polarizer exhibit several blind spots. These blind spots are due to different type of guided modes that couple to the Floquet modes. Raising the distance between the polarizer and the patch surface can eliminate some of the blind spots.
- Between the two polarizers considered, the meander-line polarizer has a better scanning capability than the strip-line polarizer, because the strip-line polarizer shows blind spots near the boresight scan angle. However, by adjusting the patch-array cell size, the blind spots can be moved away from the boresight direction.

APPENDIX
SUBARRAY IMPEDANCE MATRIX

Suppose there are $M \times N$ identical elements in a subarray of an infinite array structure. We first consider rectangular lattices for the subarray and the elements within the subarray. At the end, we will outline the procedure for a general subarray structure. Suppose V_j be the input voltage of the jth element of the subarray, where $1 \leq j \leq MN$. Also we assume that the jth element is placed at mth row and nth column of the subarray where $m \leq M$ and $n \leq N$. Therefore, the index j represents a set of two indexes $\{m, n\}$, which we symbolically denote as $j \Leftrightarrow \{m, n\}$. Any arbitrary voltage vector of MN elements can

be expressed as a linear combination of MN independent vectors. Suppose we choose the independent vectors as the Floquet excitation[3] vectors as follows:

$$
\begin{bmatrix} V_1 \\ V_2 \\ \cdot \\ \cdot \\ V_{MN} \end{bmatrix} = V_{F1} \begin{bmatrix} x_{11} \\ x_{12} \\ \cdot \\ \cdot \\ x_{1,MN} \end{bmatrix} + V_{F2} \begin{bmatrix} x_{21} \\ x_{22} \\ \cdot \\ \cdot \\ x_{2,MN} \end{bmatrix}
$$
$$
+ \cdots + V_{F,MN} \begin{bmatrix} x_{MN,1} \\ x_{MN,2} \\ \cdot \\ \cdot \\ x_{MN,MN} \end{bmatrix} \tag{25}
$$

where $V_{Fi}x_{ij}$ is the voltage excitation of the jth element where $j \Leftrightarrow \{m_j, n_j\}$. The index i is associated to a scan angle. We choose the scan angles such that the $[x_i]$ vectors become mutually orthogonal. This will allow us to find the coefficients V_{Fi} $(i = 1, 2, \cdots, MN)$ directly by means of orthogonal relations. To that end we choose the following differential phasing for the ith Floquet excitation:

$$
\{\phi_{xi}, \phi_{yi}\} = \{(\phi_x + 2(m_i - 1)\pi)/M, \\
(\phi_y + 2(n_i - 1)\pi)/N\} \tag{26}
$$

with periodicity $[a/M, b/N]$. Therefore, an element in the $[x_j]$ vectors in (25) is given by

$$
x_{\alpha\beta} = \exp\left[-j\left\{\frac{m_\beta}{M}(2(m_\alpha - 1)\pi + \phi_x) \\
+ \frac{n_\beta}{N}(2(n_\alpha - 1)\pi + \phi_y)\right\}\right] \tag{27}
$$

with $\alpha \Leftrightarrow \{m_\alpha, n_\alpha\}$, $\beta \Leftrightarrow \{m_\beta, n_\beta\}$. Equation (25) can be expressed in terms of the matrix notations

$$
[V] = [X][V_F] \tag{28}
$$

where $[X]$ is a square matrix, with $[x_j]$ vectors as columns. The Floquet coefficient vector $[V_F]$ can be determined as

$$
[V_F] = [X]^{-1}[V]. \tag{29}
$$

Now, $[X]^{-1} = [X^*]^t(1/MN)$, because $[x_j]$ vectors are orthogonal. So far, we have shown that any arbitrary excitation can be expressed as a superposition of several Floquet excitations. This Floquet excitation allows us to treat the entire array as an infinite periodic structure with periodicity $[a/M, b/N]$. For each

[3]A Floquet excitation is equivalent to *eigen vector* excitation, because the active input impedances are identical for all elements. Such an active impedance (here the Floquet impedance) essentially is equal to the *eigenvalue* of the impedance matrix.

Floquet excitation, we can find the Floquet current for each element, which is related via Floquet admittance Y_{Fj} as follows:

$$
[I_{Fj}] = Y_{Fj}V_{Fj}[x_j]. \tag{30}
$$

The total current vector is the superposition of the individual Floquet current vector. Mathematically,

$$
[I] = \sum_{j=1}^{MN}[I_{Fj}]. \tag{31}
$$

Combining (29)–(31), we obtain

$$
[I] = (1/MN)[X][Y_F][X^*]^t[V] \tag{32}
$$

where $[Y_F]$ is a diagonal matrix, the diagonal elements being the Floquet admittances associated with different scan angles. The admittance matrix of the subarray elements then becomes

$$
[Y] = (1/MN)[X][Y_F][X^*]^t. \tag{33}
$$

The impedance matrix, therefore, becomes

$$
[Z] = (1/MN)[X][Z_F][X^*]^t \tag{34}
$$

where $[Z_F]$ is the Floquet impedance matrix (diagonal). Equation (20) is a special case of (34). Expanding (34), we obtain the mutual impedance between two elements as

$$
Z_{\alpha\beta} = \frac{1}{MN}\sum_{i=1}^{MN} Z_{F,i}x_{i\alpha}x_{i\beta}^*. \tag{35}
$$

Substituting $x_{i\alpha}$ and $x_{i\beta}$ using (27), we obtain (36), shown at the bottom of the page. For large M and N we write

$$
Z_{\alpha\beta} \approx \frac{1}{4\pi^2}\sum_{m_i=1}^{M}\sum_{n_i=1}^{N} Z_{F,i}\exp\{-j2m_i(m_\alpha - m_\beta)\pi/M\} \\
\times \exp\{-j2n_i(n_\alpha - n_\beta)\pi/N\}\frac{2\pi}{M}\frac{2\pi}{N}. \tag{37}
$$

Using integral notation

$$
Z_{\alpha\beta} = \frac{1}{4\pi^2}\int_0^{2\pi}\int_0^{2\pi} Z_F(\psi_x, \psi_y) \\
\times \exp(-j\psi_x m_x - j\psi_y n_y)\,d\psi_x\,d\psi_y \tag{38}
$$

where $m_x = m_\alpha - m_\beta$, $n_y = n_\alpha - n_\beta$, and $\{\psi_x, \psi_y\}$ represents the differential-phase pair with respect to a scan angle. The above integral relation between Floquet impedance and mutual impedance of array elements was derived independently using Fourier series approach [16].

The above formulation is applicable for rectangular subarrays with inside elements arranged in rectangular lattice. However, the results can be extended for an arbitrary element-lattice structure and for a general subarray shape. It can be shown that

$$
Z_{\alpha\beta} = \frac{1}{MN}\sum_{i=1}^{MN} Z_{F,i}\exp\left[-j\left\{\frac{(m_\alpha - m_\beta)}{M}(2(m_i - 1)\pi + \phi_x) + \frac{(n_\alpha - n_\beta)}{N}(2(n_i - 1)\pi + \phi_y)\right\}\right] \tag{36}
$$

any subarray geometry is reducible in the form of a parallelogram without altering the inside elements. Consider the array in Fig. 3. Temporarily imagine the thick-line parallelogram as a general subarray geometry. For analyzing this subarray, the Floquet excitation vectors required in (25) can be constructed following the procedure in Section II-C. The kth element of the ith excitation vector $[x_i]$ is given by

$$x_{ki} = \exp(-jk'_{xm}x'_k - jk'_{yn}y'_k) \qquad (39)$$

where k varies from 1 to (ab/a_ib_i) ($=$ number of elements in a subarray), (x'_k, y'_k) is the coordinate of the kth element in $(x' - y')$ coordinate system of Fig. 3, and (k'_{xm}, k'_{yn}) are the wave numbers given in (19a). The procedure in Section II-C yields (ab/a_ib_i) distinct sets of wave numbers. The excitation vectors thus formed are mutually orthogonal, therefore, (34) can be used directly to find the mutual impedance of the subarray elements for a given scan angle.

ACKNOWLEDGMENT

The author would like to thank O. Fordham for the measured results. He would also like to thank G. Goyette and J. St. Marie for their comments to improve the presentation.

REFERENCES

[1] K. C. Gupta and A. Benalla, *Microstrip Antenna Design*. Norwood, MA: Artech House, 1988.
[2] R. J. Mailloux, *Phased Array Antenna Handbook*. Norwood, MA: Artech House, 1994, p. 275.
[3] D. M. Pozar and D. H. Schaubert, *Microstrip Antennas*. Piscataway, NJ: IEEE Press, 1995.
[4] R. Q. Lee, K. F. Lee, and J. Bobinchak, "Characteristics of a two-layer electromagnetically coupled rectangular patch antenna," *Electron. Lett.*, vol. 23, no. 20, pp. 1070–1072, Sept. 1987.
[5] Y. Lubin and A. Hessel, "Wide-band, wide-angle microstrip stacked-patch-element phased arrays," *IEEE Trans., Antennas Propagat.*, vol. 39, pp. 1062–1070, Aug. 1991.
[6] H. Legay and L. Shafai, "New stacked microstrip antenna with large bandwidth and high gain," *Proc. Inst. Elect. Eng.—MAP*, vol. 141, pp. 199–204, June 1994.
[7] J. T. Aberle, D. M. Pozar, and J. Manges, "Phased array of probe-fed stacked microstrip patches," *IEEE Trans. Antennas Propagat.*, vol. 42, pp. 920–927, July 1994.
[8] R. Mittra, C. H. Chan, and T. Cwik, "Techniques for analyzing frequency selective surfaces—A review," *Proc. IEEE*, vol. 76, pp. 1593–1615, Dec. 1988.
[9] R. S. Chu and K. M. Lee, "Analytical model of a multilayered meander line polarizer plate with normal and oblique plane-wave incidence," *IEEE Trans., Antennas Propagat.*, vol. AP-35, pp. 652–661, June 1987.
[10] J. D. Vacchione and R. Mittra, "A generalized scattering matrix analysis for cascading FSS of different periodicities," *IEEE AP-S Int. Symp. Dig.*, pp. 92–95, May 1990.
[11] N. K. Das and A. Mohanty, "Infinite array of printed dipoles integrated with a printed strip grids for suppression of cross-polar radiation—Part I: Rigorous analysis," *IEEE Trans. Antennas Propagat.*, vol. 45, pp. 960–972, June 1997.
[12] A. K. Bhattacharyya, "A numerical model for multilayered microstrip phased array antennas," *IEEE Trans. Antennas Propagat.*, vol. 44, pp. 1386–1393, Oct. 1996.
[13] ——, "A modular approach for probe-fed and capacitively coupled multilayered patch array," *IEEE Trans. Antennas Propagat.*, vol. 45, pp. 193–202, Feb. 1997.
[14] R. L. Haupt, "Reducing grating lobes due to subarray amplitude tapering," *IEEE Trans. Antennas Propagat.*, vol. AP-33, pp. 846–850, Aug. 1985.
[15] D. M. Pozar, "Scanning characteristics of infinite array of printed antenna subarrays," *IEEE Trans. Antennas Propagat.*, vol. 40, pp. 666–674, June 1992.
[16] A. K. Bhattacharyya, "Floquet modal based analysis for mutual coupling between elements in array environment," *Proc. Inst. Elect. Eng.—MAP*, vol. 144, pp. 491–497, Dec. 1997.
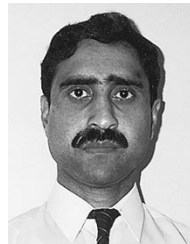
Arun K. Bhattacharyya (M'87–SM'91) was born in India in 1958. He received the B.Eng. degree in electronics and telecommunications engineering from Bengal Engineering College, University of Calcutta, India, in 1980 and the M.Tech. (microwave engineering) and Ph.D. degrees from Indian Institute of Technology, Kharagpur, India, in 1982 and 1985, respectively.

From November 1985 to April 1987, he was with the University of Manitoba, Canada, as a Postdoctoral Fellow in the Electrical Engineering Department. From May 1987 to October 1987 he worked for Til-Tek Limited, Kemptville, ON, Canada, as a Senior Antenna Engineer. In October 1987 he joined the University of Saskatchewan, Canada, as an Assistant Professor of Electrical Engineering Department. He was promoted to the Associate Professor rank in 1990. He joined the Hughes Space and Communications Company, Los Angeles, CA, in July 1991. Currently, he holds a Senior Scientist position there. He is the author of *Electromagnetic Fields in Multilayered Structures, Theory and Applications* (Norwood, MA: Artech House, 1994). His technical interests include applied electromagnetics, printed antennas, multilayered structures, active phased arrays, and modeling of microwave circuits and components.

Dr. Bhattacharyya is a recipient of the 1996 Hughes Technical excellence award.